2022-09

Energetics of tidally induced internal waves over isolated seamount

Stashchuk, Nataliya

http://hdl.handle.net/10026.1/19918

10.1016/j.wavemoti.2022.103014
Wave Motion
Elsevier

Highlights

Energetics of tidally induced internal waves over isolated seamount

Nataliya Stashchuk and Vasiliy Vlasenko

- The study focuses on the tidal energy conversion to internal waves over an isolated seamount.
- Sensitivity runs were conducted in a wide range of the numerical grid resolution.
- The coarse grid models overestimate available potential energy converted to internal waves.

Energetics of tidally induced internal waves over isolated seamount

Nataliya Stashchuk and Vasiliy Vlasenko

The University of Plymouth, UK, Plymouth, Drake Circus, PL4 8AA

Abstract

Tidally generated internal waves over Rosemary Bank Seamount, North Atlantic, were investigated using the Massachusetts Institute of Technology general circulation model. The model results were validated against in-situ data collected during the 136th cruise of the RRS 'James Cook' in June 2016. The current study focuses on the sensitivity of the model output to the parameter settings. The estimates of the available potential energy integrated over the model domain were taken as a proxy for evaluating the sensitivity of the model results to the grid steps, horizontal and vertical viscosity, diffusivity, and mixing schemes. It was found that coarse grid models overestimate available potential energy converted to internal tides over seamounts. In fact, the energy conversion rate from barotropic to baroclinic tidal components is sensitive to the grid resolution. The reasons for this tendency are discussed in the paper.

Keywords:
Internal tide, Rosemary Bank Seamount, Numerical modelling

1. Introduction

The principal sources of the tidal energy conversion from barotropic to baroclinic motions are located over oceanic ridges, continental slopes and seamounts. These areas provide a basic income to the baroclinic wave energy, which ultimately converts into internal water mixing and provides the conditions for setting the global oceanic circulation (Munk and Wunsh, 1998).

Analysis of the parameterization of internal wave effects for setting the global oceanic stratification was recently estimated by MacKinnon et al.

(2017). The authors discussed tidally induced mixing over bottom obstacles and estimated how much tidal energy is radiated to the far-field with internal waves. The lee wave mechanism of internal wave generation was the focus of this study. This scenario takes place under supercritical tidal conditions when the tidal flow is strong enough to arrest the generated internal waves in the area of topographic features. The modelling results presented by MacKinnon et al. (2017) assume that further steps in the parameterization of water mixing are required for making the model predictions accurate. A very detailed analysis of the tidal energy conversion and contribution of higher baroclinic modes to the energy balance was conducted recently by Vic et al. (2019). Using a semi-analytical model, the authors found that higher baroclinic tidal modes can account for up to 27% of tidal energy conversion.

Note that coarse-grid ocean models cannot resolve internal lee waves and short-scale internal modes. As a consequence, these processes are missing in model energy estimates. However, the comparison of fine and coarse resolution model outputs can evaluate the effect of the sub-grid baroclinic process on the energy budget. The model settings can be the same except for the grid resolution in both cases. Such experiments help understand the role of small-scale processes in water mixing and energy budget.

The present paper focuses on Rosemary Bank Seamount (RBS) located in the North Atlantic, Figure 1. This case study aims to understand the sensitivity of model predictions to the model settings. 136th cruise of the RV "James Cook" was conducted in the RBS area in May-June 2016 (hereafter JC136). The data collected during this cruise are considered in the present paper. Specifically, we refer to the temperature, salinity, temperature and velocity profiles recorded at three CTD-LADCP stations (Connectivity-Temperature-Depth, Lowered-Acoustic-Doppler-Current-Profiler). The positions of oceanographic stations are shown in Figure 1 a.

Theoretical analysis of the tidally induced internal waves around RBS was reported in (Stashchuk and Vlasenko, 2021). It was found there that internal wave dynamics, specifically, the wave generation and their propagation over RBS, can be treated in terms of two waveguides located in the seasonal and main pycnoclines, Figure 1 a. Specifically, the tidal flow interacting with a cluster of volcanic origin tall bottom cones located at the RBS summit (see Figure 1 a) generates short-scale internal waves in subsurface 100 m thick seasonal pycnocline layer. Below 800m depth, i.e. in the main pycnocline, Figure 1 b, oscillating tidal flow generates bottom trapped sub-inertial internal waves propagated counterclockwise around RBS.

The numerical experiments reported in (Stashchuk and Vlasenko, 2021) revealed a good agreement between the model and observational data. The present study is based on the concept of two waveguides reported in the paper mentioned above. The intensification of the baroclinic tidal signal in the surface and bottom layers is evident both in observations (Figure 2 a,b) and the model outputs (Figure 2 c,d).

The present study focuses on the requirements that should be applied to large-scale modelling. In many global ocean models, the horizontal grid resolution is relatively coarse,several kilometres in the best-case scenario. The model requirements for simulations of tidally induced baroclinic motions are more demanding. In many cases, the horizontal grid resolution should be 100 m or less for accurate replication of generated internal waves. The global oceanic models are incapable of simulating internal tides with such grids on global and regional scales (Robertson, 2006). We consider the RBS area as a case study in the context of broader applications of the modelling efforts.

Structure wise, the paper is arranged as follows. It starts with the model description. This section is followed by a discussion of the baroclinic tidal energy estimation method. The grid resolution and the turbulent mixing parameterizations are discussed in the section "Model results". Finally, the principal outcomes of the study are formulated in the concluding section.

2. The model

The modelling experiments were conducted using the fully non-linear non-hydrostatic Massachusetts Institute of Technology general circulation model (MITgcm) (Marshall et al., 1997). The model domain, Figure 1 a, included a 815×698 numerical grid with horizontal resolution 115 m in its central part. A telescopic increase of the spatial resolution was arranged by adding extra 128 grid points to the lateral boundaries of the calculation area. In doing so, a smooth increase of the horizontal resolution from 115 m in the central part to $2{\cdot}10^8$ m at the periphery allowed to avoid the wave reflection from the model boundaries. The water depth was restricted by 2000 m isobath in the vertical direction. The vertical grid step was ten metres in all numerical experiments.

The shaved cell method for the topography interpolation was used in the present study. Its advantage, compared to the traditional full step representation, is in the reduction of numerical errors induced by the incorrect bathymetry interpolation. This problem was discussed by Adcroft et al.

(1997). It was demonstrated there that the shaved cell method for the topography interpolation shows a substantial improvement in the consistency of the model results with the observational data compared with the traditional full step topography representation. The partial cell capability can be used with the variable parameter called in the MITgcm as $hFacMin$ (value between 0 and 1). It corresponds to the minimum fractional size of the cell. In the present calculation, we have been using $hFacMin$=0.2.

The tide forcing was activated in the model by a tidal potential added to the right-hand side of the momentum balance equations. The details of the method are described in (Vlasenko and Stashchuk, 2021). Considering that M_2 tidal signal predominates in the RBS area, we restricted our analysis using only principal semidiurnal tidal forcing. The tidal input parameters were set using the data taken from the inverse tidal model TPXO 8.0 (Egbert and Erofeeva, 2002). The model was run with a steady, uniform horizontal stratification assuming no initial horizontal pressure gradients.

The Richardson number dependent parametrization, PP81, was used for the coefficients of vertical viscosity A^h and diffusivity K^h (Pacanowski and Philander, 1981). The details are as follows:

$$\begin{aligned} A^v &= \frac{A_0^v}{(1+a\mathrm{Ri})^n} + A_b^v, \\ K^v &= \frac{A^v}{(1+a\mathrm{Ri})} + K_b^v. \end{aligned} \tag{1}$$

Here Ri is the Richardson number, $\mathrm{Ri} = N^2(z)/(u_z^2 + v_z^2)$, and u and v are the components of zonal and meridional horizontal velocities, respectively. The background mixing/viscosity model parameters A_b and K_b were set at the minimum level to provide the conditions for internal waves generation and propagation: A_b^v=$10^{-5}\,\mathrm{m}^2\ \mathrm{s}^{-1}$ and K_b^v=$10^{-5}\ \mathrm{m}^2\ \mathrm{s}^{-1}$. The adjustable parameters were: A_0^v=$1.5{\cdot}10^{-2}\,\mathrm{m}^2\ \mathrm{s}^{-1}$, a=5 and n=1. This set of model parameters revealed the excellent performance of the MITgcm in replication of tidally generated internal waves (Stashchuk et al., 2014; Stashchuk and Vlasenko, 2017; Vlasenko et al., 2014, 2018).

The PP81 parameterization increases the coefficients A^v and K^v in the areas with small Richardson numbers, which dumps shear instabilities and smooths inverse water stratification produced by breaking internal waves. It also allows setting the upper limit of the vertical viscosity coefficient A^v_{max}. In this study A^v_{max} was taken at the level of $0.1\,\mathrm{m}^2\mathrm{s}^{-1}$.

The vast majority of the model runs in this study were conducted for the time interval of six days (144 hours) with the constant horizontal viscosity

A^h and diffusivity K^h coefficients equals $0.5\,\mathrm{m}^2\,\mathrm{s}^{-1}$. Additional sensitivity runs were done in a wide range of diffusivity/viscosity parameters. They are discussed below.

Computing wise, one-hour outputs were arranged for all three-dimensional fields. In addition, vertical profiles of temperature and horizontal velocities were recorded with one-minute sampling at some selected points. Their positions coincide with the CTD-LADCP stations.

3. Tidal energy estimation method

The tidal energy conversion rate from barotropic to baroclinic component depends on many factors. They are the intensity of the tidal flow, water stratification, the shape of bottom topography, background mixing processes, etc. The sink of tidal energy to internal waves and ultimately to water mixing can be quantified in terms of internal tidal energy generated over the bottom topography.

In many cases, it is not easy to separate the barotropic tidal signal from the baroclinic one. Specifically, this is true when velocities are recorded over an inclined three-dimensional bottom topography. In this case, the separation procedure can introduce a significant error.

The residual currents generated by tides can lead to extra uncertainty in the calculations of a vertical mean tidal velocity. Specifically, this concerns the case of bottom trapped waves. Such a case was reported by Lerczak et al. (2003) who studied internal wave dynamics at the Mission Beach (USA). Analysing the ADCP data, they found differences in the structure of alongshore and cross-shore tidal currents. The authors pointed out that separating the barotropic tidal signal from the baroclinic one should be used with caution, particularly in regions with significant topographic variations. Note that the estimates of available potential energy produced by tides are less sensitive to the barotropic component. The analysis presented below is based on the estimation of the APE.

Several methods are used for the APE calculations. A comprehensive analysis of the procedures applied to internal wave fields was presented by Kang and Fringer (2010). Three commonly used methods for the APE estimates suggested by Lorenz (1955), Gill (1982), and Holliday and McIntyre (1981) are considered in this paper. It was found that the method reported by Holliday and McIntyre (1981) is the most accurate in the calculation of the APE for internal waves. Their technique is based on the Taylor series analysis. The recommended formula for the APE estimates is as follows:

$$\mathrm{APE} = \frac{g^2\rho'^2}{2\rho_0 N^2} + \frac{g^3(N^2)_z\rho'^3}{6\rho_0^2 N^6} + O(\rho'^4). \qquad (2)$$

Here ρ' is the perturbation of density to its equilibrium state.

Algorithm (2) was used in this paper. The APE calculations were conducted every one hour using the model outputs. The graphs are presented below in the following sections. Technically, the APE was calculated by vertical and horizontal integration over the whole model domain. The quadratic polynomial fit that includes the three nearest grid points best fits for the volume integrated APE and presents the long-term trend

4. Model results

The sensitivity of the model output to the horizontal and vertical grid resolution is reported in this section. The principal point of this study is: what the horizontal and vertical grid steps Δx and Δz should be taken to resolve the baroclinic tidal processes correctly? Vitousek and Fringer (2011) have shown that the ability of the model to reproduce small-scale nonhydrostatic physical processes depends on the leptic ratio coefficient, $\lambda \equiv \Delta x/h_1$. Here h_1 is the depth of the interface/pycnocline. For an accurate replication of the internal wave dynamics produced by non-hydrostatic models, the value of the leptic ratio λ should be at the level of $O(1)$ (Vitousek and Fringer, 2011).

Considering these requirements, one should mention that the water stratification in the RBS area has two principal elements shown in Figure 1 b: a shallow 100-metre depth seasonal pycnocline and the main pycnocline located below 1000 m depth. The latter is weaker but occupies a much larger part of the water column.

Numerically wise, both values of h_1 for seasonal and main pycnoclines can be taken to estimate the leptic ratio. These estimates can help in the choice of the model resolution. The principal question is: what processes should be replicated by the model? The fine resolution modelling allows considering a wide variety of small-scale dynamics, both short-scale internal waves developed in seasonal pycnocline and bottom trapped internal tidal waves. These requirements are not always possible for global-scale models. We consider a range of grid settings to illustrate models' abilities to replicate the wide-scale baroclinic tidal motions. The study discusses fine-scale resolution model experiments and analyses the coarser grid runs used in global ocean models.

4.1. Sensitivity to the grid resolution

An example of the model sensitivity to the grid resolution is shown in Figure 3. The model temperature time-series at station 32 (Figure 1 a) was calculated with different horizontal grid steps, 111.75 m, 463 m, and 926 m. They are presented in panels a, b, and c of Figure 3, respectively. This figure reveals that the ability of the model to capture short internal waves in the upper seasonal pycnocline layer decreases with the increase of horizontal grid steps. However, the numerical scheme still works well with coarser resolution and reproduces long wave oscillations. Note that long-term wave amplitudes increase with the increase of the horizontal grid steps.

How sensitive are the tidally induced baroclinic motions and water mixing to the model resolution? The coarser grid model predictions of internal tidal energy could differ from that estimated in the fine-resolution experiments. The influence of the horizontal step on the value of APE is illustrated in Figure 4 a. Here a six-day time series of the depth-integrated model domain APE calculated for the horizontal resolution Δx=Δy=111.75 m, 463 m, and 926 m are presented. The parameters $A^h = K^h$ in these experiments were $0.5\,\mathrm{m}^2\,\mathrm{s}^{-1}$, and the vertical resolution Δz was equal to 10 m.

The common feature of all three graphs is the evidence of tidal periodicity. The fit curves to these periodical oscillations show the steady growth of the APE. However, after six days of tidal motion, the system ultimately arrives at a stationary state.

The coarser grids usually dump short internal waves, which reduces the APE in the numerical predictions. At the same time, coarser grids do not affect the generation of long internal waves, which are more energetic than short-scale waves. To have some quantitative estimates, a series of numerical experiments with different grid resolutions, horizontal and vertical, was conducted to study the sensitivity of the model outputs to the model grid parameters.

The APE time series for a wide range of model resolution with horizontal grid steps from 115 m to 926 m, and vertical grid steps from 5 m to 20 m are presented in Figures 4 a and 4 b. These figures show the spin-up of the model over about 150 hours. The model comes to a stationary regime at the end of this time interval, although the domain integrated APE is sensitive to the model resolution. It is generally higher at coarser grids.

There are several explanations for this result. The first one can be found considering the domain volume. The latter is sensitive to the grid resolution. It varies with changing vertical and horizontal model grid steps, Figure 4 c and 4 d. The MITgcm is a Z-coordinate model which approximates the bottom as a step-wise function. The bottom topography in Z-coordinate models and the total water volume varies depending on the grid resolution. For instance, the total volume of water in the model domain for the coarser experiment shown in Figure 4 exceeds the fine-resolution volume for more than 2%. In addition, the topography in the coarser grid is steeper. The increase of the bottom steepness results in the generation of more energetic bottom-trapped internal waves, Figure 3.

The confirmation of the APE growth due to roughening of topography is seen in Figure 4 b. It shows the domain-integrated APE time series for three different vertical grid steps, 5 m, 10 m, and 20 m. Quantitatively, decreasing the vertical resolution in Z-coordinate models increases the water volume in the regions of sloping topography. As a result, the total APE calculated at coarser grids is higher, Figure 4 d. Making the vertical resolution thinner leads to improvements in the replication of the bottom flow dynamics.

Considering some local characteristics (not the domain integrated), the sensitivity of the model output to the grid resolution can be more detailed. Two examples of this sensitivity are shown in Figure 5. The model predicted temperature calculated at the positions of CTD stations 31 and 33 shows the consistency of all time-series considered with different horizontal and vertical grid resolutions. The tidal nature of vertical oscillations is clearly seen in these records. All curves reveal in-phase tidal periodicity. The amplitudes of vertical oscillations for all model outputs are also comparable. That could be evidence that coarse grid models can capture the main energy contributor with acceptable accuracy. At the same time, decreasing horizontal and vertical model resolution introduces some more details that can be very important for predicting local marine environment parameters.

4.2. Sensitivity to horizontal mixing parameterization

The time series of the model predicted APE calculated for different model settings, e.g. diffusivity, viscosity and grid resolution, are compared in this section. By making the grid finer, at some stage the model output starts to be insensitive to further reduction of the grid step.

Figures 6 shows the domain integrated APE and its best fit for different values of the viscosity coefficients: 0, 0.01, 0.5, 50 $\mathrm{m^2 s^{-1}}$. All curves presented here show that the tidal energy increases gradually after the model starts. The spin-up period, 150 hours, is shown in Figure 6. The system becomes stationary when the pumping tidal energy is balanced by dissipation. As we found, the model predicted volume integrated APE capacity in the area does depend on the horizontal mixing parameterization. For the horizontal mixing/viscosity coefficients between $0.01\,\mathrm{m^2s^{-1}}$ and $50\,\mathrm{m^2s^{-1}}$ the APE level varies in the range of 100 %, Figure 6. This fact should be taken into account in the interpretation of large-scale circulation modelling results.

4.3. Experiments with vertical mixing schemes

In large-scale models, the energy cascading along the spectrum is generally provided, introducing parameterization schemes for vertical viscosity and diffusivity. One of them is the Richardson number based parameterization (1) included in the MITgcm package as a standard option. It shows a good performance for internal tide modelling in many studies, e.g. Vlasenko et al. (2014, 2016, 2018); Vlasenko and Stashchuk (2018).

Field measurements (Polzin et al., 1997) have revealed that vertical mixing does not occur uniformly over the oceans. It is normally enhanced near rough topographies due to the generation of internal waves that convert to turbulence. The lower level background mixing develops at the level of $\sim 10^{-5}\mathrm{m^2s^{-1}}$ over the whole ocean interior (Ledwell et al., 1998; Gregg, 1989). This value can be three orders of magnitude larger **over rough topography features**, (Polzin et al., 1997). To have a comparison, the results presented below show the model outputs calculated for two MITgcm build-in vertical mixing schemes. In all experiments, the horizontal grid resolution was 463 m.

4.3.1. Richardson number dependent scheme PP81

The Richardson number dependent parameterization for vertical mixing (1) was used in this study. The value 0.1 $\mathrm{m^2\,s^{-1}}$ of the maximum permissible viscosity coefficient A^v_{max} was taken in this study. This requirement is applied in the MITgcm setting for the areas with strong vertical mixing, assuming possible density inversions. Note that the background turbulent mixing was set at the level of A^v_b=$10^{-5}\,\mathrm{m^2\ s^{-1}}$ and K^v_b=$10^{-5}\ \mathrm{m^2\ s^{-1}}$ in the whole area.

The sensitivity of the model outputs to the viscosity coefficient A^v_{max} was checked by changing this parameter within a two-order range. The result is shown in Figure 7. It illustrates that the increase of A^v_{max} from 0.001 to 0.1 $\mathrm{m^2\,s^{-1}}$ leads to stabilizing of the model output. Comparing the time series of temperature records calculated for Station 32 with different $A^v_{\rm max}$ coefficients, Figures 7 a and 7 b, indicates that the choice $A^v_{\rm max}$=0.1 m^2 s^{-1} shows a more stable model output.

4.3.2. KL10 mixing scheme

Klymak and Legg (2010) developed an original mixing scheme that is focused on the effect of breaking internal waves and does not include the Richardson-number criterion. This scheme assumes that energy dissipation is governed by the equivalence of the density overturning scales to the Ozmidov scale. Eddy diffusivity and viscosity are estimated using the Osborn relation (Osborn, 1980). This method yields a simple parameterization $Kz = 0.2L_T^2N$, where L_T is the size of vertical density overturns. This method is included in the MITgcm as the KL10 package. It was scrutinized by Klymak et al. (2013) that this parameterization does not account for shear-driving mixing.

A series of experiments were conducted in the present study with KL10 mixing scheme. An example of typical time series of the APE calculated for station 32 is shown in Figure 7 c. For the comparison, panels a and b show similar time series calculated using the PP81 scheme with different maximum permissible viscosity coefficients A^v. All other model parameters were the same in these experiments.

Note that at a local scale, a two-order decrease of the maximum vertical viscosity coefficient results in the appearance of instabilities that are visible in the time series, Figure 7 b. Comparison of Figures 7 a and 7 b indicates that the choice $A^v_{\rm max}$=0.1 m^2 s^{-1} is the more realistic one producing a more stable vertical structure (without inversions) usually observed in the ocean. The KL10 parameterization reproduces both long-period internal waves in the bottom layer and short-period waves in the surface layer quite successfully, Figure 7 b, although the signal looks less regular than that produced by the PP81 scheme, Figure 7 a.

Figure 8 b shows the APE time series obtained with the PP81 and KL10 schemes. Both APE curves are close to each other over 93 hours of the model run. However, after eight tidal cycles, the APE calculated using the KL10 scheme continues to grow above the already saturated APE level achieved by the PP81-scheme.

5. Discussion and conclusions

Tidal energy conversion from barotropic to baroclinic components is one of the principal driving forces of the global ocean mixing and meridional overturning circulation (Munk and Wunsh, 1998). This process is still not well resolved in global ocean models. Specifically, the question is to what extent the tidal energy conversion is sensitive to the models' settings. Grid resolution, vertical turbulent mixing parameterization, and horizontal viscosity/diffusion settings are critical for a robust model prediction.

In previous studies, the authors achieved a good agreement between the model outputs and field observations (Stashchuk et al., 2014; Stashchuk and Vlasenko, 2017; Vlasenko et al., 2014, 2018). In this paper, a similar range of input model parameters is used. In the RBS area, the comparative analysis of model results and in situ data collected during JC136 cruise was reported in (Stashchuk and Vlasenko, 2021). The consistency of the model outputs with the in-situ collected data was demonstrated. The present paper considers the problem in a broader context, assuming that large-scale numerical models usually use coarse numerical grids and can not include fine-scale baroclinic processes. The present paper estimates the possible effect of numerical grid resolution and turbulent mixing parameterization schemes on the model output. The principal aim was to find the range of the model applicability and its sensitivity to the input parameter settings.

It was found that the increase of the grid step leads to a damping of the generation of short internal waves. This result was entirely expected, assuming higher numerical viscosity at coarser grids. A surprising outcome was the increase of the domain integrated APE at coarser numerical grids. The answer was found in terms of the model topography variations presented at different grid resolutions. Z-coordinate numerical models reproduce the bottom topography steeper at coarser grids, affecting the model performance and intensifying the generated waves.

The estimates of the tidally induced kinetic energy (K) accumulated in the area over one tidal cycle has shown the following results: $K = 3.814{\cdot}10^{13}$J for the grid $\Delta x = \Delta y =$115.75 m, $K = 3.8337 \cdot 10^{13}$J for the grid $\Delta x = \Delta y =$463 m, and $K = 4.0357 \cdot 10^{13}$ J for the grid $\Delta x = \Delta y =$926 m. The vertical resolution dz and the background horizontal viscosity A_b^v were the same in all these experiments, i.e. $dz = 10$ m and $A_b^v = 0.5m^2s^{-1}$, respectively. Thus, it was found that both available potential energy and the kinetic energy increase in the model outputs on coarser grids.

The energy conversion rate from barotropic tidal component to internal waves in the RBS area was estimated. The calculations were conducted using the methodology suggested by Kelly et al. (2010); Zhang et al. (2017). The energy conversion EC for the domain $L_x \times L_y$ was calculated as:

$$EC = \int_0^{L_x} \int_0^{L_y} \left\langle p' \vec{U} \nabla H \right\rangle dxdy. \quad (3)$$

Here $\langle . \rangle$ means the time-averaging over one tidal cycle, $\vec{U}$ is the depth-averaged horizontal velocity, and p' is the wave-induced pressure perturbation. It was found that EC =3.35·10^8 W for a grid $\Delta x = \Delta y$ =115.75 m, EC =3.32·10^8 W for the grid resolution $\Delta x = \Delta y$ =463 m, and EC =2.97·10^8 W for the grid $\Delta x = \Delta y$ =926 m. The vertical step for all considered experiments was the same, equals Δz =10 m. Our experiments clearly show that the energy conversion rate from surface tides to baroclinic motions is underestimated in coarser grid experiments.

A similar analysis of the sensitivity of the energy conversion rate to the horizontal grid spacing was conducted by Niwa and Hibiya (2011) (for Global Ocean) and Zilberman et al. (2009) (for the Mid-Atlantic Ridge). These authors used quite a different numerical approach than applied in the present paper. Specifically, the terrain-following sigma-coordinate hydrostatic models were applied to these calculations. It was found there that the tidal energy conversion rate integrated over the global ocean (Niwa and Hibiya, 2011) and local area in the Brazil Basin (Zilberman et al., 2009) increases with the reduction of the model grid spacing. This conclusion is in line with the results reported here obtained by using the $z-$coordinate MITgcm model.

A methodological outcome from this study is that simple estimations of the available potential energy and the total kinetic energy generated by the tides over RBS show the increase of these values on coarser model grids, Figure 6 a and b. At the same time, the estimates of the energy conversion rate from barotropic to internal tide reveal that the coarser grids reduce the efficiency of the tidal energy conversion. There is no contradiction between these two tendencies. Analysis of Figure 4 c and 4 d shows that the coarser grids incorporate larger volumes of water with the increase of the grid step. In fact, with the coarser grids, the topography's tidal activity is different from that simulated over the fine-resolution topography.

A series of numerical experiments were also conducted to test the model output's sensitivity to the choice of diffusivity/viscosity model coefficients.

Water mixing parameterization is critical for accurately modelling various processes, from microscopic to global atmospheric and oceanic scales. In the present study, we used the Richardson-number dependent parameterization scheme PP81. This turbulent closure scheme provides the APE saturation over eight tidal cycles. The Osborn relation based scheme KL10 also revealed a similar performance over 7.5 tidal periods. Note that its further performance over ten tidal cycles did not demonstrate any tendency to reach the stationary level. In general, the usage of two vertical turbulent mixing schemes, PP81 and KL10, did not significantly differ the model output over several tidal cycles, although the KL10 closure model shows a higher internal tidal energy saturation level.

6. Acknowledgement

This work was supported by the Natural Environment Research Council (NERC) [grant NE/K011855/1]. The authors thank the University of Plymouth Research Computing Service staff for their support.

References

Adcroft, A., C. Hill, and J. Marshall (1997) Representation of topography by shaved cells in a height coordinate Ocean Model. *Monthly Weather Review*, *125(9)*, 2293-2315, doi:10.1175/1520-0493(1997)125¡2293:ROTBSC¿2.0.CO;2.

Baum J.K., R.A. Maiers, D.G. Kehler, B.Warm, S.Harley, and P.Doherty (2003) Collapse and conservation of shark populations in the Northwest Atlantic. *Science*, *299*, 389–392.

Egbert, G.D., and S.Y. Erofeeva (2002) Efficient inverse modeling of barotropic ocean tides, *J. Atmos. Oceanic Technol., 19(2)*, 183–204.

Gill, A.E. (1982) Atmosphere-Ocean Dynamics. Academic Press, 662pp.

Gregg, M.C. (1989) Scaling turbulent dissipation in thermocline. *J. Geophys. Res., 92*, 5249-5286.

Hampton J., J.R. Sibert , P. Kleiber, M.N. Maunder, S.R. Harley (2005) Fisheries: Decline of Pacific tuna populations exaggerated? *Nature*, *434*, E1–E2.

Holliday, D., and M.E. McIntyre (1981) On potential energy density in an incompressible fluid. *J. Fluid Mech., 107*, 221-225.

Kang, D., and O. Fringer (2010) On the calculation of avalable potential energy in internal wave fields. *J. Phys. Oceanogr.*, *40*, 2539-2545.

Kelly, S.M., J.D. Nash, and E. Kunze (2010) Internal-tide energy over topography. *J. Geophys. Res.*, *115*, C06014, doi:10.1029/2009JC005618.

Klymak, J.M., and S.M. Legg (2010) A simple mixing scheme for models that resolve breaking internal waves. *Ocean Modelling*, *33*, 224-234.

Klymak, J.M., M. Buijsman, S. Legg, and R. Pinkel (2013) Parameterizing surface and internal tide scattering and breaking on supercritical topography: the one- and two-ridge cases.*J. Phys. Oceanogr.*, *43*, 1380-1397.

Ledwell,J.R., A.J.Watson, and C.S.Law (1998) Mixing of the tracer in the pycnocline. *J. Geophys. Res.*, *103*, 21499-21529.

Lerczak, J.A., and C.D. Winant, and M.C. Hendershott (2003) Observations of the semidiurnal internal tide on the southern California slope and shelf. *J. Geophys. Res., 108(C3)*, doi:10.1029/2001JC001128.

Lorenz, E.N. (1955) Available potential energy and the maintenance of the general circulation. *Tellus*, *7*, 157-167.

Marshall, J., A. Adcroft, C. Hill, L. Perelman, and C. Heisey (1997), A finite-volume, incompressible Navier-Stokes model for studies of the ocean on parallel computers. *J. Geophys. Res.*, *102*, 5733-5752.

MacKinnon, J. A. et al. (2017) Climate process team on internal-wave driven ocean mixing. *Bull. Am. Meteor. Soc.*, *98*, 2429-2454.

Munk W. and C. Wunsh (1998) Abyssal recipes II: energetics of tidal and wind mixing *Deep Sea Res.*, *45*, 1997-2010.

Myers, N, R.A. Mittermeier, C.G.Mittermeier, G.A.B. da Fonseca, J.Kent (2000) Biodiversity hotspots for conservation priorities. *Nature*, *403*, 853–858.

Myers R.A., B. Worm (2003) Rapid worldwide depletion of predatory fish communities. *Nature* *423*, 280–283.

Niwa, Y., and T. Hibiya (2011) Estimation of baroclinic tide energy available for deep ocean mixing based on three-dimensional global numerical simulations. *J. Oceanogr.*, *67*, 493-502.

Osborn, T.R.(1980) Estimates of the local rate of vertical diffusion from dissipation measurements. *J. Phys. Oceanogr.*, *10*, 83-89.

Pacanowski, R.C., and S.G.H. Philander (1981) Parameterisation of vertical mixing in numerical models of Tropical Oceans. *J. Phys. Oceanogr.*, *11*, 1443-1451.

Plozin, K.L., J.M.Toole, J.R. Ledwell, and R.W.Schmitt (1997) Spatial variability of turbulent mixing in the abyssal ocean. *Science*, *276*, 93-96.

Robertson, R. (2006). Modeling internal tides over Fieberling Guyot: Resolution, parameterization, performance. Ocean Dynamics, 56, 430– 444. https://doi.org/10.1007/s10236-006-0062-5.

Roberts, C.M. (2002) Priorities for tropical reefs marine biodiversity hotspots and conservation. *Science*, *295*, 1280–1284.

Stashchuk, N., V. Vlasenko, M.E, Inall, and D. Aleynik (2014) Horizontal dispersion in shelf seas: High resolution modelling as an aid to sparse sampling. *Progr. Oceanogr.*, *128*, 74-87.

Stashchuk, N., and V. Vlasenko (2017) Bottom trapped internal waves over the Malin Sea continental slope. *Deep-Sea Res. I*, *119*, 68-80.

Stashchuk, N., V. Vlasenko, P. Hosegood, and A.W. Nimmo-Smith (2017) Tidally induced residual current over the Malin Sea continental slope. *Cont. Shelf. Res.*, *139*, 21-34.

Stashchuk, N., V. Vlasenko, and K. L. Howell (2018) Modelling tidally induced larval dispersal over Anton Dohrn Seamount. *Ocean Dyn.*, *68(11)*, 1515-1526.

Stashchuk, N., and V. Vlasenko (2021) Internal wave dynamics over isolated seamount and its influence on coral larvae dispersion. *Fronties.*, *123(9)*, 6753-6765.

Vic, C., A. C. Naveira Garabato, J. A. M. Green, A. F. Waterhouse, Z. Zhao, A. Melet, C. de Lavergne, M. C. Buijsman, and G. R. Stephenson (2019) Deep-ocean mixing driven by small-scale internal tides. *Nature Communications*—, 10, 2099, doi.org/10.1038/s41467-019-10149-5.

Vitousek, S. and O.B. Fringer (2011) Plysical vs. numerical dispersion in nonhydrostatic ocean modeling. *Ocean Model.*, *40*, 72-86.

Vlasenko, V., N. Stashchuk, M.E. Inall, M. Porter, and D. Aleynik (2016) Focusing of baroclinic tidal energy in a canyon. *J. Geophys. Res.*, *121(4)*, 2824-2840.

Vlasenko, V., N. Stashchuk, W.A.M. Nimmo-Smith (2018) Three-dimensional dynamics of baroclinic tides over a seamount. *J. Geophys. Res.*, *123(2)*, 1263-1285.

Vlasenko, V., and N. Stashchuk (2018) Tidally induced overflow of the Faroese channels bottom water over the Wyville Thomson Ridge. *J. Geophys. Res.*, *123(9)*, 6753-6765.

Vlasenko, V., and N. Stashchuk (2021) Setting tidal forcing for regional modelling of internal waves. *Ocean modelling*, *160*, 101767. https://doi.org/10.1016/j.ocemod.2021.101767. bibitem[Vlasenko et al.(2005)]Vletal2005 Vlasenko, V., N. Stashchuk, and K. Hutter (2005) Baroclinic tides: theoretical modeling and observational evidence. Cambridge University Press.

Vlasenko, V., N. Stashchuk, M.E. Inall, and J. Hopkins (2014) Tidal energy conversion in a global hot spot: On the 3-D dynamics of baroclinic tides at the Celtic Sea shelf break. *J. Geophys. Res.*, *119*, doi:10.1002/2013JC009708.

Worm B, H.K. Lotze, R.A. Myers (2003) Predator diversity hotspots in the blue ocean. Proc. Natl. Acad. Sci. USA 100:9884–9888.

Zhang, L., M.C. Buijsman, E. Comino, and H. L. Swinney (2017) Internal wave generation by tidal flow over periodically and randomly distributed seamounts. *J. Geophys. Res.*, *122*, 5063-5074, doi:10.1002/2017JC012884.

Zilberman, N. V., and J. M. Becker, M. A. Merrifield, and G. S. Carter (2009) Model estimates of M2 internal tide generation over Mid-Atlantic Ridge topography. *J. Phys. Oceanogr.* , *39(10)*, 2635-2651, doi:10.1175/2008JPO4136.1

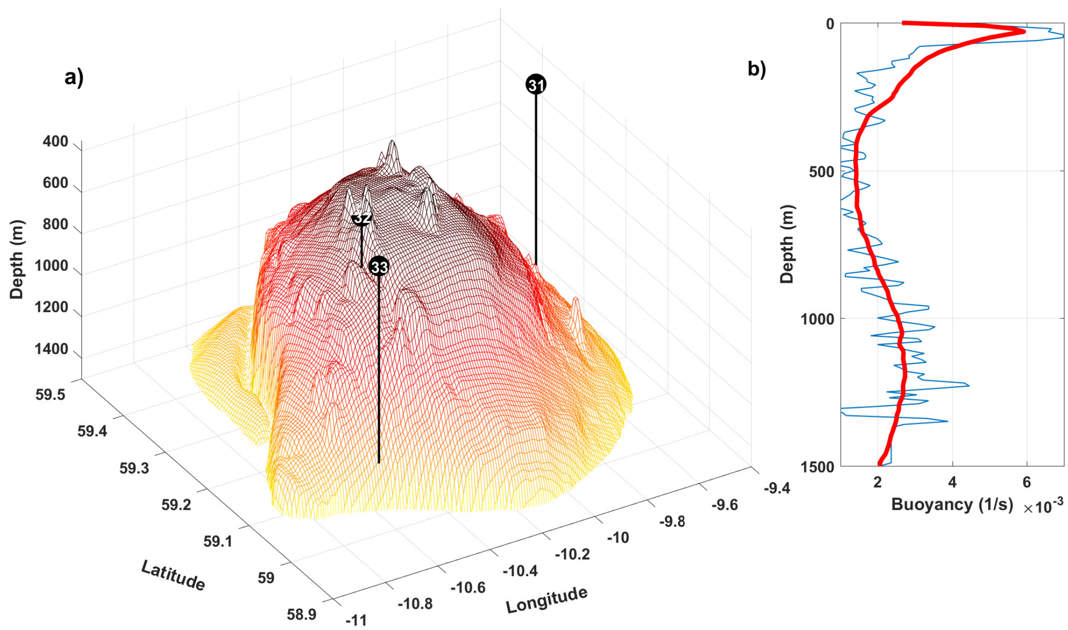

Figure 1: a) Bottom topography of Rosemary Bank Seamount (RBS) with the location of CTD stations 31, 32, and 33 conducted during the 136th cruise of the RV "James Cook". b) The buoyancy frequency recorded in the RBS area is shown in blue. The smoothed buoyancy frequency profile used in the modelling is shown in red.

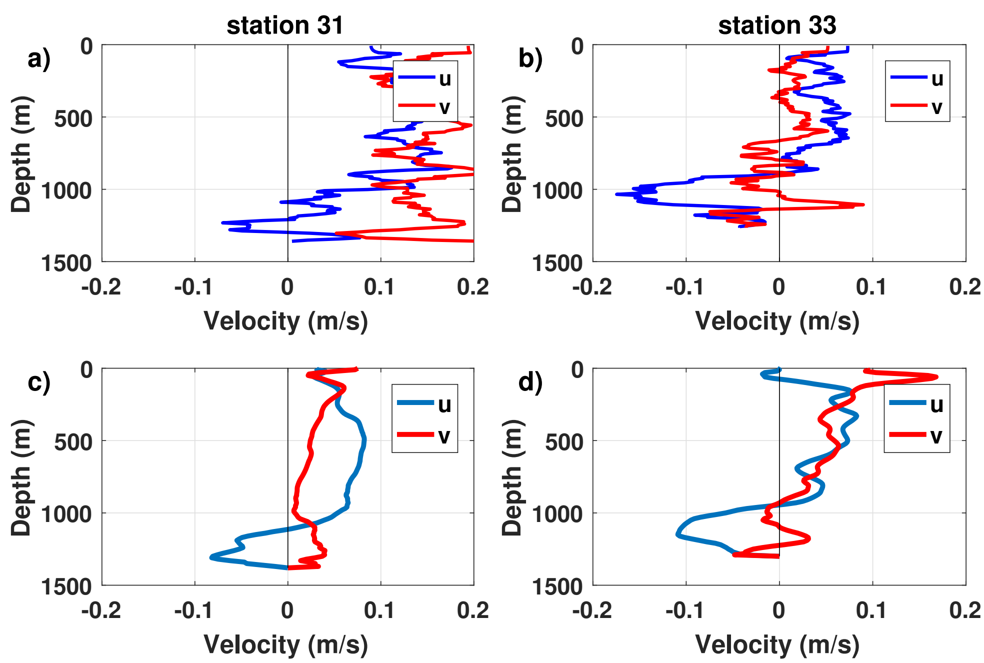

Figure 2: Vertical profiles of zonal (blue) and meridional (red) velocities recorded by the LADCP at 31-st and 33-rd CTD stations (panels a and b, respectively). Panes c and d present the same profiles but replicated by the numerical model.

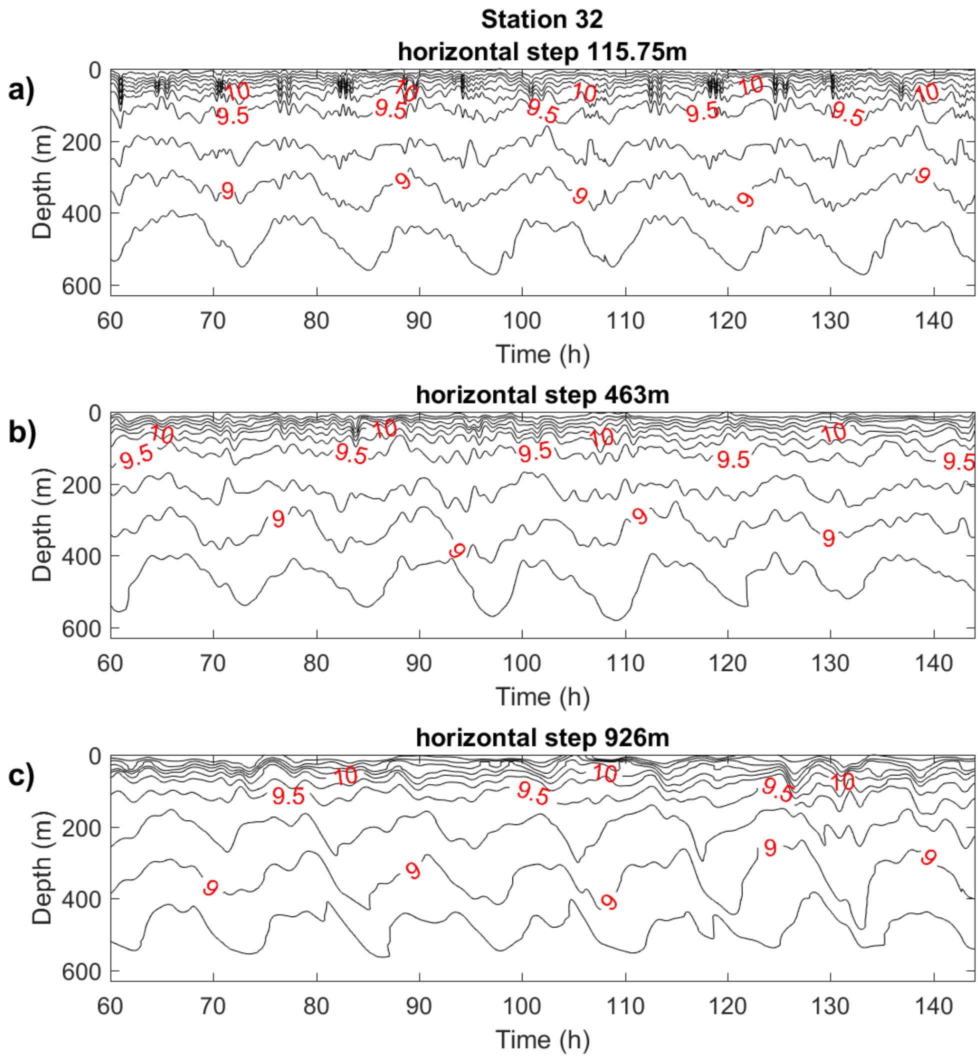

Figure 3: Temperature time series reproduced by the MITgcm at the 32-nd CTD station (the position is shown in Figure 1). The horizontal grid step in these experiments was 115.75 m, 463 m, and 926 m (panels a, b, c, respectively).

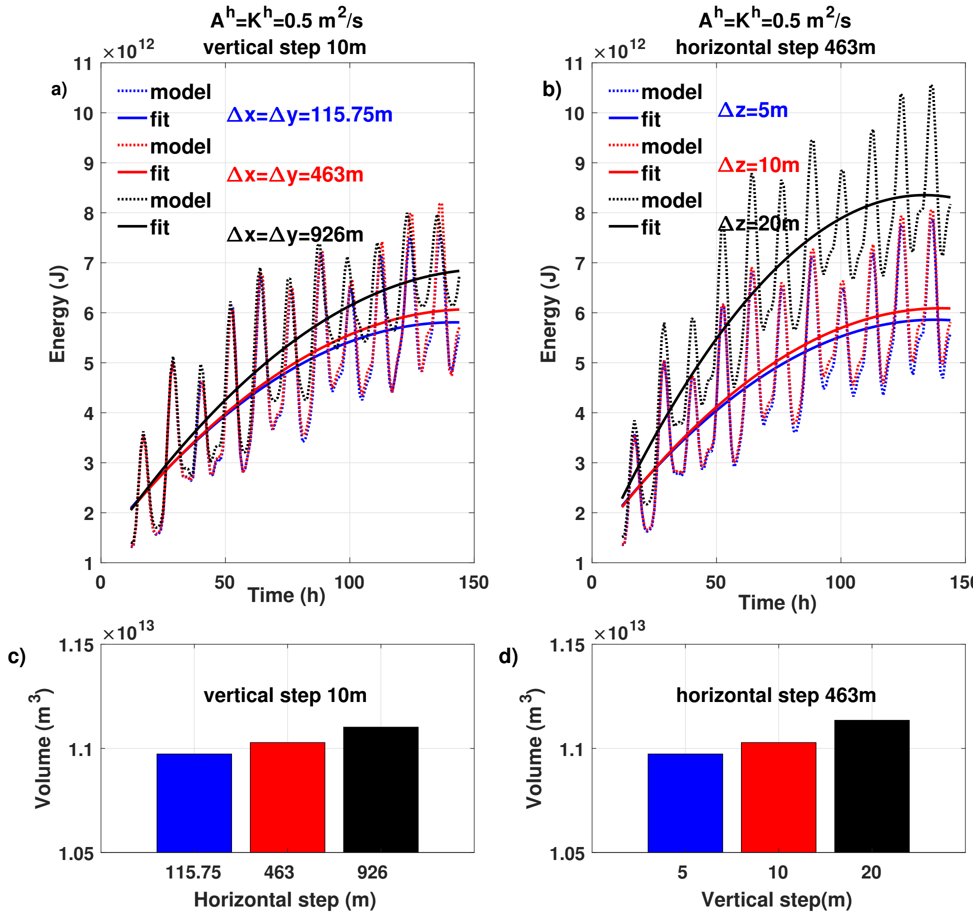

Figure 4: a) Model predicted available potential energy (APE) calculated for the RBS area with a different vertical grid resolution: 115.75m (blue), 463m (red) and 926m (black). b) The same, but calculated with different vertical steps: 5m (blue), 10m (red) and 20m (black). c) and d) The volume of the model domain calculated for different horizontal and vertical grid resolutions. The values are shown in the graph.

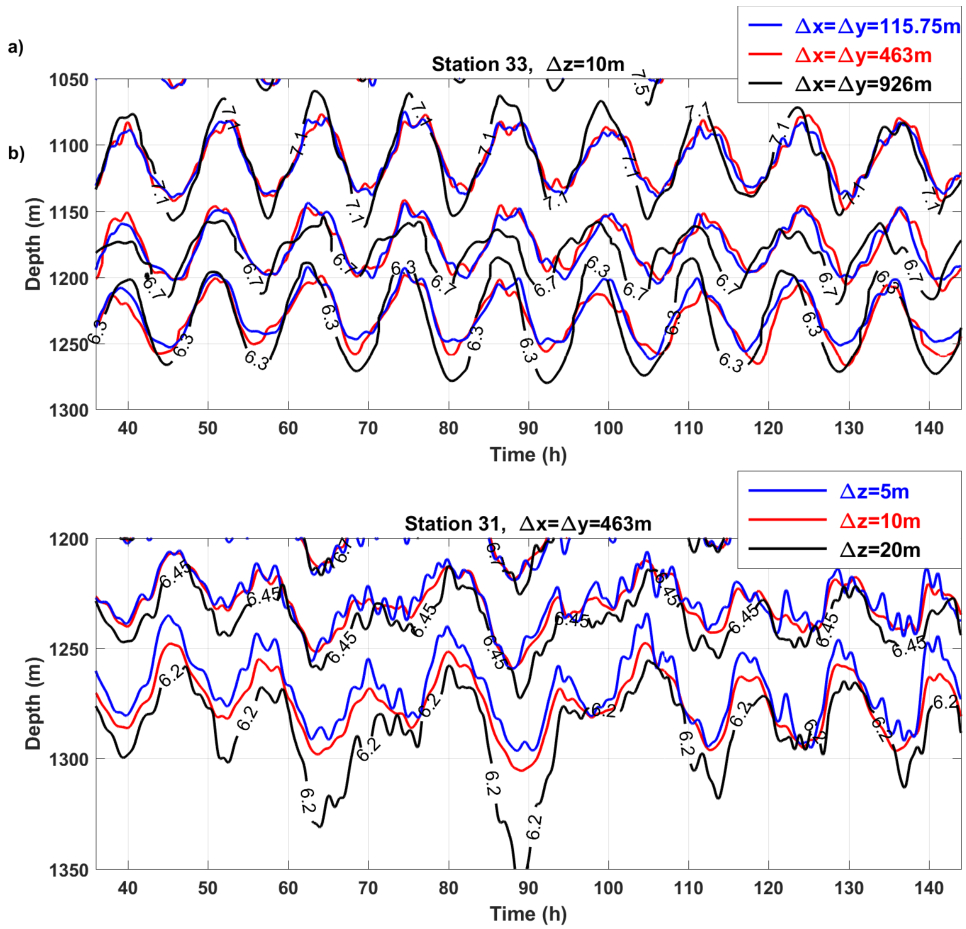

Figure 5: The model predicted time series at stations 33 a) and 31 b) for different horizontal a) and vertical b) grid steps. The model resolution is detailed in the figure legend.

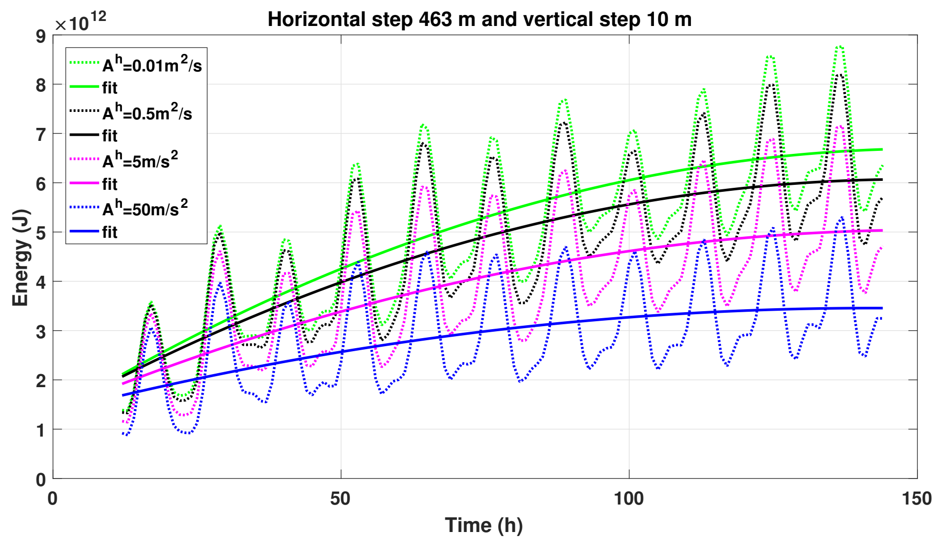

Figure 6: The domain integrated APE calculated for different values of horizontal viscosity coefficient.

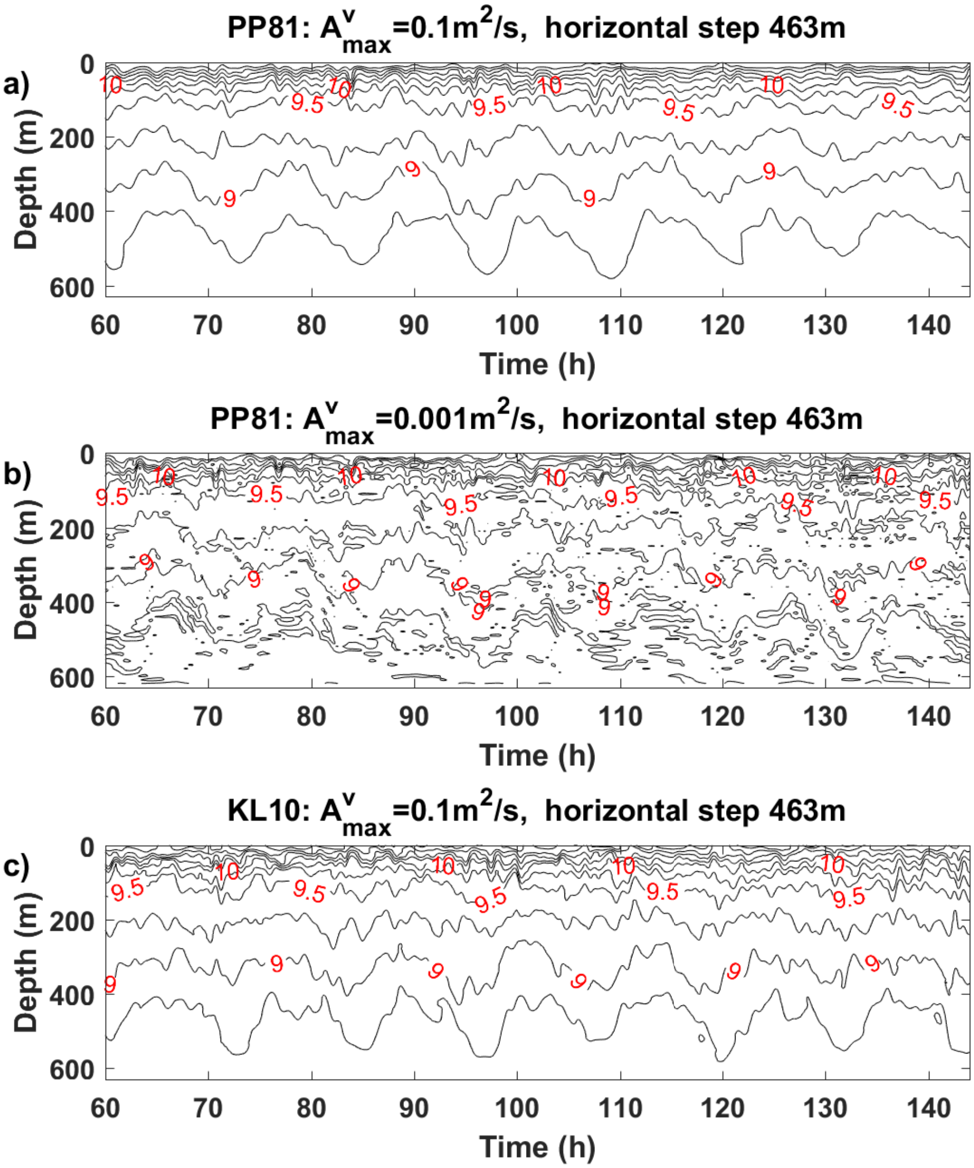

Figure 7: Sensitivity runs conducted with different vertical mixing parameterization schemes. The model predicted temperature time series were calculated for the point of CTD station 32 (Figure 1).

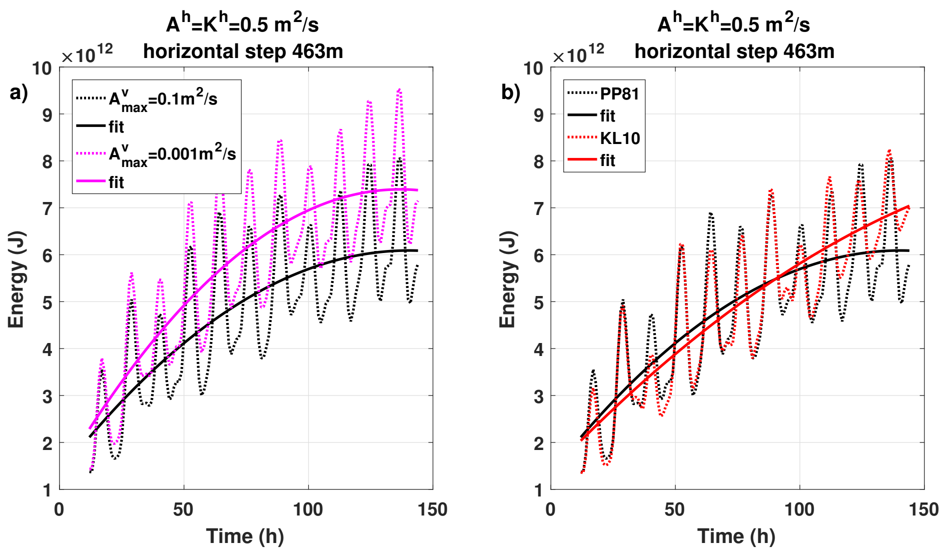

Figure 8: The domain integrated APE time series for different viscosity coefficients and parameterization schemes (Pacanowski and Philander (1981) and Klymak et al. (2013)) calculated at the position of CTD station 32.